Carbon 174 (2021) 368–381

Contents lists available at ScienceDirect

Carbon

journal homepage: www.elsevier.com/locate/carbon

Research Article

Tetrahex carbides: Two-dimensional group-IV materials for nanoelectronics and photocatalytic water splitting

Mehmet Emin Kilic *, Kwang-Ryeol Lee **

Computational Science Research Center, Korea Institute of Science and Technology, Seoul, 02792, Republic of Korea

ARTICLE INFO

Article history:
Received 24 July 2020
Received in revised form
2 December 2020
Accepted 3 December 2020

Keywords:
2D materials
Photocatalytic water-splitting
Auxetic materials
Two dimensional carbides
First-principle calculations
Group-IV carbides

ABSTRACT

We report a series of novel two-dimensional (2D) group-IV carbides with perfectly ordered arrangement of tetragons and hexagons. The 2D tetrahex carbides possess robust energetic, dynamical, thermal, and mechanical stabilities. They have strong anisotropic mechanical, electronic, and optical properties. The negative Poisson's ratio (PR) in the 2D tetrahex carbides emerges by small tensile strain (2–5%). The feature of sign-tunable PR enables them to be non-auxetic, auxetic, and partially-auxetic nanomaterials. They exhibit ultrahigh ideal strength that can even outperform graphene. They are natural semiconductors with direct and indirect band gaps which can be tuned by strain engineering. Beyond the binary carbides, the ternary alloying of group-IV elements further provides the ability to engineer their structural, mechanical, optical, and electronic properties. Excitingly, the alloying offers a continuous band gap energy, band edge modulation, and indirect-to-direct band gap transition. The 2D tetrahex-carbides exhibit high and directionally anisotropic carrier mobility, favorable for the separation of photogenerated carriers, and has very good optical absorption performance in the visible-light region. The position of band edges in the 2D tetrahex carbides fits perfectly the water oxidation and reduction potentials. Therefore, the 2D tetrahex carbides have potential applications not only in photocatalytic water-splitting but also in designing 2D opto-electro-mechanical devices.

1. Introduction

Two-dimensional (2D) materials exhibit distinctive electronic, optical, and mechanical properties that are absent in their bulk counterparts, making them highly desirable for versatile applications in energy storage and photocatalysis [1–4]. In recent years, 2D photocatalysts for hydrogen generation from the direct splitting of water have attracted a great deal of attention due to their unique inherent advantages enhancing catalytic performance: (i) very high surface to volume ratio providing much more adsorption sites for OH^-, H^+, and H_2O participating in the photocatalytic reaction, and making the surface more reactive and (ii) the relatively short carrier transport distance, improving photo-induced electronâ€“hole migration and separation, and reducing their recombination rate. Several experimental studies have indicated that the advantages of 2D materials are helpful to improve the photocatalytic activity compared to bulk materials [5–7]. For instance, the photocurrent density for 2D SnS_2 was reported to be over 70 times higher than that of bulk SnS_2 [8] while for ZnSe nanosheet it was found to be 200 times higher than that of bulk ZnSe [9].

Group-IV mono-elemental materials as the most obvious alternatives for graphene have become a promising and versatile class of 2D materials. Silicene as the Si counterpart of graphene has been predicted theoretically [10–13] and fabricated experimentally on various kinds of substrates, including Ag [14], ZrB_2 [15], and Ir [16]. The Ge counterpart of silicene, namely germanene, was first proposed in 2009 [13] and successfully synthesized on Au [17] and Pt [18] in 2014. Stanene, the Sn-based analog of graphene, has been synthesized on Bi_2Te_3 surface [19]. The electronic band structures of silicene, germanene, and stanene are quite similar to those of graphene, in which the zero-gap semi-metallic behavior with Dirac cones at Fermi energy appears [13,20]. Contrary to graphene, these three graphene-like 2D materials prefer to construct sp^3-like hybridized orbitals rather than sp^2 ones due to their larger atomic radius. They exhibit slightly buckled structures, leading to very promising applications, such as an electrically tunable band gap, topological phase transition, and a quantum-spin Hall effect [21,22]. Beyond the group-IV mono-elemental 2D materials, their

* Corresponding author.
** Corresponding author.
E-mail addresses: mekilic@kist.re.kr (M.E. Kilic), krlee@kist.re.kr (K.-R. Lee).

https://doi.org/10.1016/j.carbon.2020.12.003
0008-6223/

binary compounds such as SiC, GeC, and SnC have attracted extensive research interest due to their unique properties [23,24]. The 2D binary carbides with honeycomb structures possess band gaps, making them desirable for nano-electronic applications. For instance, graphene-like silicon carbide ($h-$SiC) exhibits a large direct band gap and an exciton binding energy of up to 2.0 eV [25], which is desirable for optoelectronic device applications, such as LEDs or solar cells. Significant experimental and theoretical efforts have been devoted to the synthesis of $h-$SiC, stimulating an intense quest for novel 2D compounds of Si and C atoms [26–31].

Of late, the most considerable attention has kept on the preparation of graphene-like carbides, however, they are not the only possible metastable 2D structures for the group-IV carbides [32]. In the quest of new functional 2D materials with unprecedented properties is among the most research attention. Very recently, great theoretical efforts have been made to investigate the electronic and mechanical properties of tetra-hexagonal carbon [33–38]. Herein, using the combinatorial lattice decoration in tetra-hexagonal carbon, we computationally designed a series of novel 2D binary and ternary carbides, containing group-IV elements (Si, Ge, Sn) which are chemically similar to carbon as they are in the same group of the periodic table with different atomic size and electro-negativity. From the first-principles calculations, the predicted 2D tetrahex carbides are composed perfectly ordered arrangement of tetragons and hexagons configurations. We revealed their energetic, dynamic, thermal, and mechanical stabilities by evaluating the formation energy, phonon dispersion, *ab-initio* molecular dynamics (AIMD) simulations, and elastic constants, respectively, which thereby suggests that the existence of the tetrahex carbides is likely. After confirming their stabilities, we systematically studied their structural, mechanical, electronic, and optical properties, and revealed their potential of utilizing for nano-electronics, solar-energy harvesting and water splitting. The ternary alloying of group-IV elements (C, Si, Ge, and Sn) and strain engineering provide the ability to engineer the inherent properties of the 2D carbides.

2. Methods

For calculations of the predicted 2D tetrahex carbides, we used the state-of-the-art first principles calculations using projector augmented wave potentials [39,40]. A plane-wave basis set, implemented in the VASP program [41], with energy cutoff value of 520 eV was used. The exchange correlation potential was approximated by the generalized gradient approximation using the functional of Perdew, Burke, and Ernzerhof (PBE) [42]. The Brillouin zone (BZ) integration was performed within Monkhorst-Pack scheme [43] by using $18\times 18\times 1$ **k**-points. A vacuum space of 20 Å was inserted along the *z*-axis, and periodic boundary conditions were applied along the *x*- and *y*-axis to study 2D systems. The atomic positions and lattice constants of the 2D carbides were optimized using a conjugate-gradient (CG) algorithm until force components on each atom were decreased below 0.010 eV/Å. The energy band gap, which was underestimated in the PBE scheme, was corrected by the Heyd-Scuseria-Ernzerhof hybrid functional (HSE06), constructed by mixing 25% of nonlocal Fock exchange with 75% of PBE exchange and 100% of PBE correlation energy [44,45]. To examine the dynamic stability of the proposed 2D carbides, the lattice dynamics calculations were performed using the Phonopy package [46]. A $4\times 4\times 1$ supercell with $2\times 2\times 1$ *k*-mesh was adopted to calculate the atomic force and the dynamical matrix, and very high accuracy (the convergence criterion of the total energy was set as 1×10^{-8} eV) To check the thermal stability of the 2D carbides, the *ab initio* molecular dynamics calculations (AIMD) were performed under constant temperature (T) and volume (V) where the temperature was controlled by using Nose-Hover thermostat [47–49]. The total simulation time for the AIMD simulations was taken 6 ps with a time step of 1 fs. For optical response calculations, we employed GW_0 approximation and the Bethe-Salpeter equation (BSE) to include electron-hole interactions [50–52]. Due to computational limit, *k*-point sampling was limited to $8\times 8\times 1$ for the GW_0, and the plane-wave cutoff energy was reduced to 480 eV. The total number of bands was increased to 144 for the GW_0 calculations.

3. Results and discussion

3.1. Atomic structures

The atomic structure of the 2D tetrahex carbides is presented in Fig. 1 (a). The tetrahex carbides are represented by the formula of $th-$XC (X = Si, Ge, $Si_{0.33}Ge_{0.67}$, $Si_{0.67}Ge_{0.33}$, $Si_{0.67}Sn_{0.33}$, $Ge_{0.67}Sn_{0.33}$) with *Pccm* symmetry (space group 49), possessing an orthorhombic lattice with constants of *a* and *b*. The structure of $th-$XC compounds is composed of four types of atoms, namely 3- and 4-fold coordinated carbon atoms (denoted as C^3 and C^4, respectively) and X atoms (denoted as X^3 and X^4, respectively) with three atomic layers. The middle layer is made of both X^4 and C^4 atoms, which are sandwiched between top and bottom layers of C^3 and X^3 atoms, respectively. Three types of atomic bond length d_1, d_2, and d_3 are defined for X^3-C^3, X^3-C^4, and X^4-C^3, respectively. Due to the structure inherent in the tetra-hexagonal lattice, we define two layer thicknesses of h_1 and h_2, which are the difference of vertical coordinates between the C^3 atoms in the top and bottom layers and the X^3 atoms in the top and bottom layers, respectively. The unique atomic structure endows the 2D carbides with exceptional mechanical, electronic, and optical properties.

For the sake of comparison, we first investigated 2D binary carbides with hexagonal ($h-$XC) and tetragonal ($t-$XC, (X = Si, Ge, Sn)) structures, where all the bonds are assigned to the X – C bonds. The obtained lattice parameters of $h-$XC compounds agree well with those obtained by Sahin et al. [24] (Figure S1 of Supporting Information). Moreover, the results of the structure parameters, phonon dispersion, and electronic band structure of the 2D tetragonal silicon carbide ($t-$SiC) agree well with the report of Fan et al. (Figure S2 (a)–(d) of Supporting Information) [53]. For 2D tetragonal germanium carbide ($t-$GeC), to our best knowledge, we first report the optimized lattice parameters, the phonon spectrum, electronic band structure, and AIMD results. We found that $t-$GeC is stable even under thermal shock (Figure S2 (e)–(h) of Supporting Information). It is noted that 2D tetragonal tin carbide ($t-$SnC) is found to be (dynamically) unstable.

We then turned out our attention to investigate the structure-property relationships and bond feature of $th-$XC compounds and compare those with $h-$XC and $t-$XC structures. In our previous work, we examined the details of structure of $th-$C [37], so we will not explain them further. For $th-$SiC, the obtained lattice constants are $a=5.531$ Å and $b=7.632$ Å. The layer thickness h_1 and h_2 are found to be 1.601 Å and 1.251 Å, respectively. The calculated bond length of Si^3-C^3 ($d_1=1.716$ Å) is comparable with that of $h-$SiC (1.788 Å). The bond length of Si^3-C^4 ($d_2=1.882$ Å) and Si^4-C^3 ($d_3=1.883$ Å) is in the range of Si – C bond length in $t-$SiC about (1.874–1.916 Å). For $th-$GeC, the corresponding lattice parameters were elongated. Such that we obtained $a=5.887$ Å, $b=8.074$ Å, $h_1=1.604$ Å, and $h_2=1.489$ Å. The bond length of d_1 (1.820 Å) is a little smaller than that of $h-$GeC (1.884 Å). The d_2 and d_3 are found to be 2.018 Å and 1.980 Å, respectively, which are comparable Ge – C bond length in $t-$GeC (2.051–2.064 Å). Hence, all these lattice parameters for $th-$GeC are higher than those of $th-$SiC. Importantly, the lattice parameters of *a* and *b* for Si – Ge –

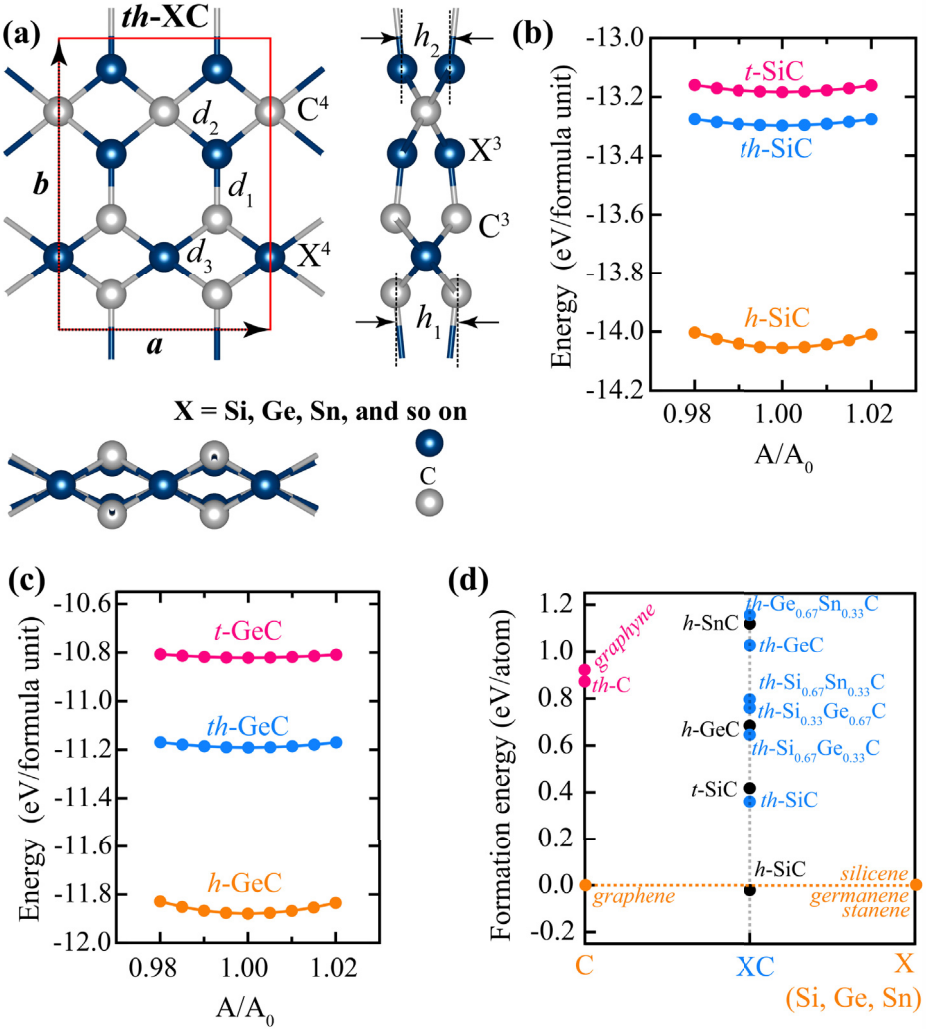

Fig. 1. (a) Top view and side views of $th-XC$ ($X = Si, Ge, Si_{0.33}Ge_{0.67}, Si_{0.67}Ge_{0.33}, Si_{0.67}Sn_{0.33}, Ge_{0.67}Sn_{0.33}$). The unit cell is depicted in red line. Blue and gray balls represent X and C atoms, respectively. X^3/C^3 and X^4/C^4 refer to as 3-fold and 4-fold coordinated atoms, respectively. (b) and (c) Total energy of hexagonal, tetragonal, and tetra-hexagonal structured silicon carbides (denoted as $h-SiC$, $t-SiC$, and $th-SiC$, respectively) and germanium carbides (denoted as $h-GeC$, $t-GeC$, and $th-GeC$, respectively). (d) The relative formation energy of *th*"TT5843c571""ADXC compounds with respect to their group-IV mono-elemental counterparts. (A colour version of this figure can be viewed online.)

C ternary alloys ($th-Si_{0.33}Ge_{0.67}C$ and $th-Si_{0.67}Ge_{0.33}C$) are in between those of $th-SiC$ and $th-GeC$. This indicates that ternary alloying of the group-IV elements provides the ability to engineer the lattice parameters of the 2D carbides. The lattice parameters, bond lengths, and thickness of $th-XC$ compounds follow the trend which is the same as the order of atomic number (or atomic radii). According to charge density distribution, the charges of $th-XC$ compounds are mainly localized at the carbon atoms (Figure S3 (a) of Supporting Information). To elucidate the nature of chemical bonds, we further analyzed the electron localization function (ELF) for the corresponding bonds in $th-XC$ compounds. According to the ELF analysis, we clearly showed the existence of σ and distorted π bonds between X^3 and C^3 atoms (Figure S3 (b) of Supporting Information). The overlapping of p_z orbitals of X^3 and C^3 atoms results in conjugated π orbitals, and causes the asymmetric distribution of wave functions around X^3 and C^3 atoms. For the X^3-C^4 and X^4-C^3 bonds, they are ionic or covalent, depending on the electronegativity difference between X and C atoms in $th-XC$.

3.2. Energetic stability

The stability of the 2D tetrahex carbides was evaluated by investigating their relative energies. First, we compared the energy of $th-XC$ compounds with $h-XC$ and $t-XC$. We found that the total energy of $th-SiC$ is 0.756 eV/(Si – C) higher than that of $h-SiC$ and 0.114 eV/(Si – C) lower than that of $t-SiC$ (Fig. 1 (b)). Likewise, the total energy of $th-GeC$ is 0.688 eV/(Ge – C) higher than that of $h-GeC$ and 0.370 eV/(Ge – C) lower that of $t-GeC$ (Fig. 1 (c)). Thus, $th-XC$ compounds are energetically in between $h-XC$ and $t-XC$. To further evaluate the energetic stability of $th-XC$ compounds, we calculated their relative formation energy. The formation energy E_f for X_nC_m structure was calculated by using $E_f = (E_{X_nC_m} - nE_X - mE_C)/(n+m)$ where $E_{X_nC_m}$, E_X, and E_C denote the total energy of X_nC_m, a single X atom in silicene for X = Si, in germanene for X = Ge, and in stanene for X = Sn, and a single C atom in graphene, respectively. The low formation energy suggests the relative stability of the 2D tetrahex carbides from their group-IV mono-elemental counterparts. The formation energy of $th-XC$ compounds is presented in Fig. 1 (d) and summarized in Table 1. It is noted that the formation energy of $th-XC$ compounds is higher than that of graphene, but energetically comparable that with other group-IV carbides. Considering the experimentally synthesized graphdyine having 0.82 eV/atom formation energy [54], the presented 2D carbides are energetically favorable than graphdiyne,

Table 1
Calculated lattice parameters a and b, thickness (or buckling height) h_1 and h_2, bond lengths d_1 for $X^3 - C^3$, d_2 for $X^3 - C^4$, and d_3 for $X^4 - C^3$ in Å, formation energy (E_f) in eV/atom, electronic band gap energy with PBE functional (E_g^{PBE}) and HSE06 (E_g^{HSE06}) method in eV, and the electronic band gap feature (Type).

	A	B	h_1	h_2	d_1	d_2	d_3	E_f	E_g^{PBE}	E_g^{HSE06}	Type
$th-C$[a]	4.533	6.107	1.160	1.160	1.340	1.540	1.540	0.87	1.62	2.63	Direct
$th-SiC$	5.531	7.632	1.601	1.251	1.716	1.882	1.883	0.36	1.09	1.78	Indirect
$th-GeC$	5.887	8.074	1.604	1.489	1.820	2.018	1.980	1.03	0.70	1.34	Indirect
$th-Si_{0.33}Ge_{0.67}C$	5.712	7.964	1.487	1.509	1.826	1.995	1.888	0.76	0.75	1.45	Indirect
$th-Si_{0.67}Ge_{0.33}C$	5.698	7.754	1.696	1.245	1.715	1.907	1.974	0.64	0.90	1.53	Indirect
$th-Si_{0.67}Sn_{0.33}C$	5.930	7.950	1.970	1.211	1.713	1.946	2.146	0.80	0.76	1.40	Direct
$th-Ge_{0.67}Sn_{0.33}C$	6.149	8.252	1.965	1.389	1.817	2.059	2.157	1.16	0.74	1.28	Indirect

[a] Ref. [37].

and indicating the possible experimental realization of the proposed 2D carbides.

3.3. Dynamic stability and phonon properties

To estimate the dynamic stability of the 2D tetrahex carbides, we performed phonon dispersion calculations using *ab-initio* lattice dynamics. Fig. 2 shows the dispersions of phonon modes for $th-C$ and $th-XC$ compounds. The unit cell consists of 12 atoms, resulting in 36 phonon modes of which 3 of them are zero-frequency acoustic branches. The transverse and longitudinal in-plane branches have a linear dispersion near the Γ point, whereas the out-of-plane branch has a quadratic dependence when q approaches 0. Harmonic approximation for dynamical stability implies a condition that all phonon modes must have real and positive frequencies. Thus, the 2D tetrahex carbides are confirmed to be dynamically stable as the phonon dispersions exhibit no negative-frequency modes. It is noted that $th-SnC$ is found to be dynamically unstable with imaginary phonon modes.

2D nanomaterials are extremely sensitive to the environmental conditions due to their inherent large surface to volume ratios. Considering the experimental realization of 2D materials, the lattice mismatch between them, substrate induced-strains, and external load or bending are the external strains on the laboratory scale. In this regard, it is necessary to further explore the dynamic (or kinetic) stability of the 2D tetrahex carbides under strain conditions. The predicted 2D tetrahex carbides were subjected to high strain (8–10% equi-biaxial tensile strain), and the phonon dispersions of the strained structures were calculated. The results showed that all the phonon modes are still positive (real) (Figure S4 of Supporting Information); and hence, the 2D tetrahex carbides remain robust even under the strain condition. To interpret the high frequency phonon modes, we plotted the atom-orbital projected phonon density of states (PhDOS) in Figure S5 of Supporting Information. According to the PhDOS results, the high frequency modes are mainly determined by the vibrations of the C^3 atoms. The highest frequency of $th-XC$ compounds is higher than that of the corresponding structure of $h-XC$. For instance, the highest frequency of $th-SiC$ (~1100 cm^{-1}) is higher than that of $h-SiC$ (about ~1000 cm^{-1}) (Figure S1 of Supporting Information), $t-SiC$ (about ~800 cm^{-1}) (Figure S2 of Supporting Information), silicene (about ~580 cm^{-1}) [13], and MoS_2 monolayer (about ~473 cm^{-1}) [55], indicating the robustness of $X^3 - C^3$ bonds in $th-XC$ lattice. Also, we note that as the atomic number of X element(s) in $th-XC$ compounds increases, the phonon bands become less dispersive.

3.4. Thermal stability

The thermal stability of the 2D tetrahex carbides was corroborated by *ab-initio* molecular dynamics simulations (AIMD) at high temperatures for 6 ps. We adopted a relatively large supercell of 4 × 3 repeated units to reduce the periodic constraints and explore the possible structure reformation. The variation of potential energy of *th*"TT5843c571""ADC and $th-XC$ compounds with time is nearly constant with fluctuations during the simulation time (Figure S6 of Supporting Information). The fluctuations in the potential energy are due to the thermal oscillations of the atoms around their equilibrium lattice positions. The snapshots of the atomic

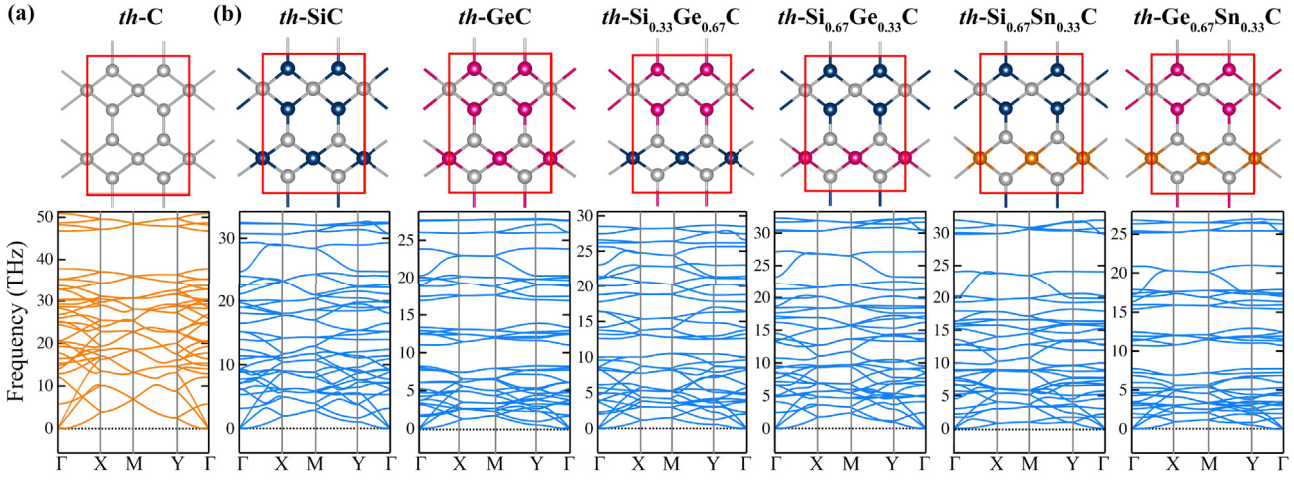

Fig. 2. (Upper panel) Optimized atomic structure of (a) $th-C$ and (b) $th-XC$ (X = Si, Ge, $Si_{0.33}Ge_{0.67}$, $Si_{0.67}Ge_{0.33}$, $Si_{0.67}Sn_{0.33}$, $Ge_{0.67}Sn_{0.33}$). Unit cells are depicted in red line. The gray, blue, pink, and orange balls represent C, Si, Ge, and Sn atoms, respectively. (Lower panel) phonon band structure of (a) $th-C$ and (b) $th-XC$ compounds along the high symmetric k points in the Brillouin zone. (A colour version of this figure can be viewed online.)

arrangements at the end of the simulation time are depicted in the inset of the figure, where there is neither bond breakage nor structure reconstruction. Therefore, even at high temperatures, the basic skeleton of the 2D carbides remains the same. Although 6 ps is a short time interval, it is long enough for the AIMD simulations. These results at least confirm that the predicted 2D tetrahex carbides are thermally stable under thermal shock.

3.5. Mechanical stability

We finally tested the strain-induced mechanical stability of the 2D tetrahex carbides by the virtue of Born-Huang elastic stability criteria [56], $C_{11}C_{22} - C_{12}^2 > 0$ and $C_{66} > 0$ where C_{11}, C_{22}, C_{12}, and C_{66} are the elastic stiffness constants calculated by fitting the second derivatives of strain energy per unit area as a function of the in-plane strains (namely, uniaxial, biaxial, and shear) via the following equations,

$$E_s(\varepsilon) = \frac{1}{2}C_{11}\varepsilon_x^2 + \frac{1}{2}C_{22}\varepsilon_y^2 + C_{12}\varepsilon_x\varepsilon_y + 2C_{66}\varepsilon_{xy}^2 \quad (1)$$

$$\text{uniaxial"TT5843c571""ADx} \rightarrow (\varepsilon_y,\ \varepsilon_{xy} = 0),\ E_s(\varepsilon) = \frac{1}{2}C_{11}\varepsilon_x^2 \quad (2)$$

$$\text{uniaxial} - y \rightarrow (\varepsilon_x,\ \varepsilon_{xy} = 0),\ E_s(\varepsilon) = \frac{1}{2}C_{22}\varepsilon_y^2 \quad (3)$$

$$\text{biaxial} \rightarrow (\varepsilon_x = \varepsilon_y), (\varepsilon_{xy} = 0),\ E_s(\varepsilon) = \left(\frac{1}{2}C_{11} + \frac{1}{2}C_{22} + C_{12}\right)\varepsilon_x^2 \quad (4)$$

$$\text{shear} \rightarrow (\varepsilon_x,\ \varepsilon_y = 0),\ E_s(\varepsilon) = 2C_{66}\varepsilon_{xy}^2 \quad (5)$$

where E_s is the strain energy per unit area, ε_x and ε_y are the infinitesimal uniaxial strains along the a and b lattice directions, respectively. Using Equation (2), C_{11} was calculated for uniaxial-x strain where the strain was only applied along the a lattice direction and defined as $\varepsilon_x = \frac{a-a_0}{a_0}$ by setting $\varepsilon_y = 0$. Likewise, C_{22} was calculated for uniaxial-y strain where the strain was only applied along the b lattice direction and defined as $\varepsilon_y = \frac{b-b_0}{b_0}$ by setting $\varepsilon_x = 0$ (see Equation (3)) where a, b and a_0, b_0 are the lattice constants with and without strain, respectively. To calculate C_{12}, the 2D systems were subjected to the equi-biaxial strain by setting $\varepsilon_x = \varepsilon_y$ using Equation (4). We note that for the equi-biaxial strain, just atomic positions are allowed to relax. Moreover, the C_{66} was calculated by Equation (5) under shear strain condition. The applied strains are sufficiently low ranging from −2% to 2% with an increment of 0.5%. We note that, when the system is subjected to the uniaxial-x or uniaxial-y strain, we simultaneously relax the other stress components to zero by considering Poisson's effect. The variation in the strain energy with the applied strain is plotted in Figure S7 of Supporting Information. The obtained elastic stiffness constants were given in Table 2. From these results, the elastic constants meet the mechanical stability criteria. Hence, the proposed 2D carbides are mechanically stable.

3.6. Mechanical properties

Having ensured that the predicted 2D tetrahex carbides are dynamically, thermally, and mechanically stable, we further investigated their mechanical properties including in-plane Young's modulus (Y), Poisson's ratio (ν), and ultimate tensile strength (UTS), which are the most important mechanical properties in relation to strain. The anisotropic geometric structure of the 2D tetrahex carbides evokes their anisotropic mechanical behavior, which is attracting interest because of offering new possibilities to achieve direction (or angle)-dependent properties. To explore this behavior, we calculated the oriented-dependent Young's modulus and Poisson's ratio of $th-$C and $th-$XC. Compounds, which can be expressed as:

$$Y(\theta) = \frac{C_{11}C_{22} - C_{12}^2}{C_{11}s^4 + C_{22}c^4 + \left(\frac{(C_{11}C_{22}-C_{12}^2)}{C_{66}} - 2C_{12}\right)s^2c^2} \quad (6)$$

$$\nu(\theta) = \frac{C_{12}(s^4 + c^4) - \left(C_{11} + C_{22} - \frac{(C_{11}C_{22}-C_{12}^2)}{C_{66}}\right)s^2c^2}{C_{11}s^4 + C_{22}c^4 + \left(\frac{(C_{11}C_{22}-C_{12}^2)}{C_{66}} - 2C_{12}\right)s^2c^2} \quad (7)$$

where $s = \sin(\theta)$ and $c = \cos(\theta)$.

3.6.1. Young's modulus

Young's modulus as an indication of stiffness is of considerable importance to study the mechanical properties of 2D materials. We examine Young's modulus of th-$th-$C and th-$th-$XC compounds along an arbitrary in-plane direction (θ) and presented in Fig. 3 (upper panels). Obviously, the 2D carbides are highly direction-dependent nanomaterials, which is due to the different strength of bonding closely related to the bond lengths and hybridization of states. The calculated Young's modulus of the 2D carbides along the x (0°) and y (90°) directions (denoted as Y_x and Y_y, respectively) are summarized in Table 2. In our previous study [37], we have reported that the Young's modulus of $th-$C (Y_x = 286.12 N/m and Y_y = 279.88 N/m) is higher than that of penta-graphene ($Y_x = Y_y$ = 263.8 N/m) [57]. Moreover, the Young's modulus of $th-$

Table 2
Calculated elastic constants C_{ij} in N/m, in-plane Young's Modulus Y_x and Y_y in N/m, Poisson's ratio ν_{xy} and ν_{yx}, and threshold values of -PR$_x$ and -PR^y (where the negative Poisson's ratio begins to emerge) in the x and y directions for $th-$C and $th-$XC compounds. Ultimate tensile strength (UTS) in % for uniaxial strain in the x and y directions and equi-biaxial strain are referred to as UTS^x, UTS^y, and UTS^{xy}, respectively. The calculated C_{ij}, Y_x, Y_y, ν_{xy}, and ν_{yx} values were calculated at small strain region range from −2 to 2% while the -PR$_x$ and -PR^y were calculated at relatively large strain range from −2% to 10%.

	C_{11}	C_{22}	C_{12}	C_{66}	Y_x	Y_y	ν_{xy}	ν_{yx}	**-PRx**	-PRy	UTSx	UTSy	UTS^{xy}
$th-$C	287.03	280.82	16.21	123.99	286.12	279.88	0.06	0.06	8	4	32	31	20
$th-$SiC	143.59	107.36	2.74	41.66	143.53	107.29	0.02	0.03	–	2	25	23	21
$th-$GeC	119.15	84.18	6.24	37.69	118.83	83.72	0.05	0.07	–	4	23	19	18
$th-$Si$_{0.33}$Ge$_{0.67}$C	126.97	97.24	5.96	36.22	126.69	96.87	0.05	0.06	–	3	24	20	18
$th-$Si$_{0.67}$Ge$_{0.33}$C	135.12	94.46	5.10	44.45	134.92	94.18	0.04	0.05	–	4	22	23	18
$th-$Si$_{0.67}$Sn$_{0.33}$C	115.86	75.95	1.88	39.53	115.83	75.91	0.02	0.02	–	2	32	21	22
$th-$Ge$_{0.67}$Sn$_{0.33}$C	99.21	66.34	1.68	34.66	99.18	66.30	0.02	0.03	–	2	27	18	22

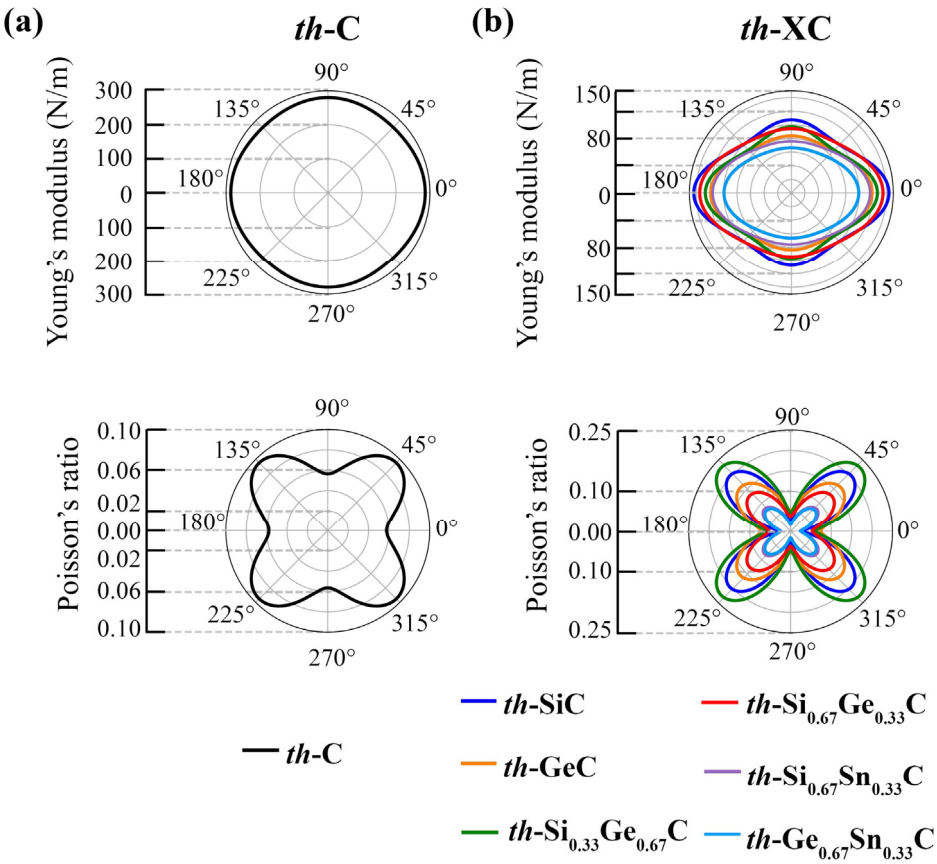

Fig. 3. Calculated orientation-dependent Young's modulus ($Y(\theta)$) (upper panels) and Poisson's ratio ($\nu(\theta)$) (lower panels) of (a) *th* – C and (b) *th*"TT5843c571""ADXC (X = Si, Ge, $Si_{0.33}Ge_{0.67}$, $Si_{0.67}Ge_{0.33}$, $Si_{0.67}Sn_{0.33}$, $Ge_{0.67}Sn_{0.33}$). (A colour version of this figure can be viewed online.)

SiC ($Y_x = 143.59$ N/m and $Y_y = 107.36$ N/m) is relatively lower than that of *h*-SiC (162.7 N/m) [58]. Likewise, for *th* – GeC, the Y_x and Y_y of *th* – GeC are found to be 118.83 N/m and 83.72 N/m, respectively, which are lower than those in *h* – GeC (143.8 N/m) [59]. Importantly, the calculated Young's modulus values of *th* – $Si_{0.33}Ge_{0.67}C$ and *th* – $Si_{0.67}Ge_{0.33}C$ are in between those of *th* – SiC and *th* – GeC, indicating the ability to engineer the Young's modulus of the 2D carbides by alloying. It is worthy noting that, the in-plane Young's modulus generally decreases with increasing the atomic number of the constituent element (X) in *th*"TT5843c571""ADXC compounds.

3.6.2. Poisson's ratio

The majority of the common solid materials possess positive Poisson's ratio (PR), which means that these materials get thinner when stretched and fatter when compressed. In contrast, a bunch of materials exhibit a negative PR, i.e, they become fatter when stretched. The list of negative PR materials, referred to as *auxetic* [60], is fairly rare [61,62]. The *auxetic* materials, as a novel class of materials, are of significant interest because of the possibility of the enhancement of the mechanical properties [60,61,63] and thus making them useful in applications, particularly in biomedical, aerospace, and defense industries [64,65]. Although considerable research efforts have been made to reveal *auxetic* materials, there are only a few studies in 2D materials with negative PR [57,66,67].

The PR of the 2D tetrahex carbides was evaluated using equation (7). We found that the PR of *th* – C and *th* – XC compounds is positive around their equilibrium state. As shown in Fig. 3, the maximum PR in *th* – C is located along the [110] direction (45°) with values of 0.09 whereas the minimum is located along the both [100] direction (or 0°) and [010] direction (or 90°) with values of 0.06. The similar behavior is also observed for *th*"TT5843c571""ADXC compounds. The feature of directionality in the PR of the 2D tetrahex carbides indicates the anisotropy of their mechanical properties.

Recently, Qiu et al. reported the emergence of negative PR in a class of 2D honeycomb structures by large tensile strain (~18% for graphene and *h*"TT5843c571""ADBN and ~33% for silicene) [68]. With this motivation, we systematically investigated the ability of the emergence of the negative PR in the predicted 2D tetrahex carbides by strain-engineering. The PR of *th* – C and *th*"TT5843c571""ADXC compounds was further calculated in the strain range from −2% to 10% by means of finite difference method [69,70] as considering the non-linear lattice response to the applied axial strain might take place. The Poisson's ratio ν_{xy}, defined as the ratio of response (or transverse) strain in the *y* direction ($\varepsilon_{\text{trans}-y} = \epsilon_y^j$) to axial strain applied in the *x* direction ($\varepsilon_{\text{axial}-x} = \epsilon_x^j$), was obtained by;

$$\nu_{xy} = \frac{\epsilon_y^{j+1} - \epsilon_y^{j-1}}{\epsilon_x^{j+1} - \epsilon_x^{j-1}} \tag{8}$$

where $j = 1, 2, \ldots$ and represents the strain increment number. Likewise, we calculated ν_{yx}, which is the ratio of response strain in the *x* direction to the applied axial strain in the *y* direction (uniaxial-*y*). The variation of transverse strain and PR of *th* – C and *th*"TT5843c571""ADXC compounds with respect to given

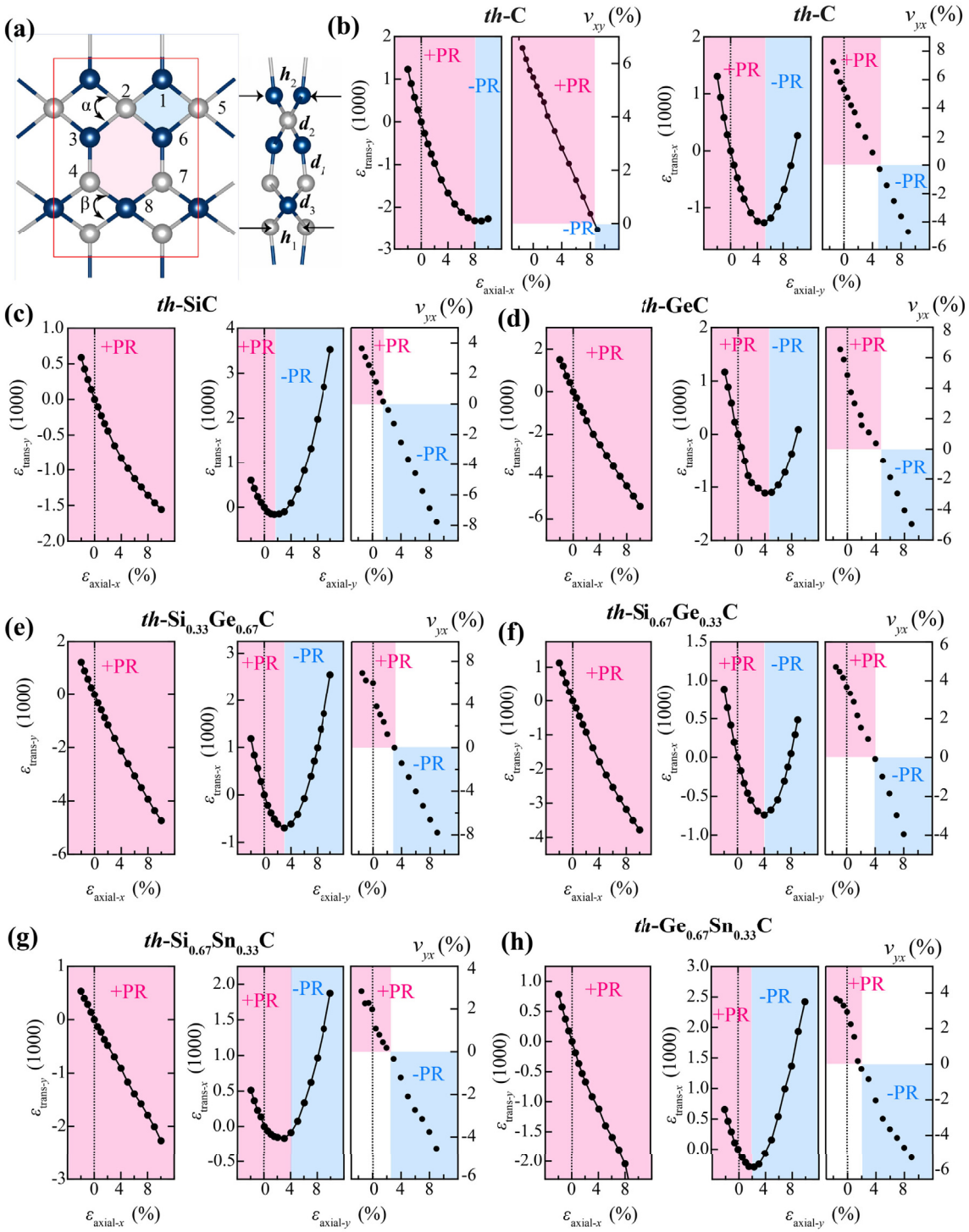

Fig. 4. Variation of transverse strain and Poisson's ratio of *th*"TT5843c571""ADC and *th*"TT5843c571""ADXC compounds with respect to given longitudinal tensile strain (uniaxial-*x* and uniaxial-*y*). The positive Poisson's ratio (+PR) shaded pink and the negative Poisson's ratio (-PR) shaded blue are depicted. (A colour version of this figure can be viewed online.)

longitudinal tensile strain (uniaxial-*x* and uniaxial-*y*) is presented in Fig. 4. For *th* – C, the response strains $\varepsilon_{\text{trans}-x}$ and $\varepsilon_{\text{trans}-y}$ monotonically decrease with the uniaxial-*y* and uniaxial-*x* strains up to the threshold values of 8% and 4%, respectively, where the response strains begin to increase (Fig. 4 (b)). Remarkably, the negative PR in *th* – C along the *x* and *y* directions simultaneously emerges when the applied strain is larger than the corresponding threshold values. Moreover, the auxetic behavior is enhanced with further strain applications. For *th*"TT5843c571""ADXC compounds, the response strain $\varepsilon_{\text{trans}-y}$ almost linearly decreases with the uniaxial-*x* strain. However, the $\varepsilon_{\text{trans}}$"TT5843c571""AD*x* monotonically decreases with the uniaxial-*y* strain up to some threshold strain values ranging from 2% to 5%, and then simultaneously increases with further strains. For instance, the negative PR in *th* – SiC and *th* – GeC simultaneously emerges at 2% and 4% uniaxial-*y* strains, respectively (Fig. 4 (c) and (d)). It is worthy noting that the threshold values, given in Table 2, for the emergence of the negative PR in *th*"TT5843c571""ADXC compounds are much more smaller

than the value of graphene, *h*"TT5843c571""ADBN, and *h* – SiC (which are close to each other about ~18%) [68], making the 2D tetrahex carbides exceptional nanomaterials in nanomechanical applications. Thus, *th*"TT5843c571""ADXC compounds exhibit non-auxetic behavior when subjected to the uniaxial-*x* strain whereas they show auxetic behavior in the presence of the uniaxial-*y* strain for the certain tensile strain values. This is called as "partially auxetic".

To understand how the negative PR emerges in the 2D tetrahex carbides, we investigated the variation of the lattice constants with respect to the applied axial strain. Within the range of the positive PR, the lattice constant *a*/*b* decreases with increasing of the applied uniaxial-*y*/uniaxial-*x* tensile strain. Further, the simultaneous increase in the *a*/*b* is expected with increasing the uniaxial-*y*/uniaxial-*x* strains for the range of negative PR. First, we investigated the underlying mechanism of the simultaneous increase in the lattice constant *b* with the uniaxial-*x* strain. The *b* is two times the projection of the bond length d_1 and the projection of the bond lengths d_2 and d_3 in the *xy*-plane. Such that, the *b* is governed by the d_1, d_2, d_3, α (the angle between two $C^4 - X^3$ bonds), β (the angle between two $C^3 - X^4$ bonds), Θ_{267} (the angle of $C^4 - X^3 - C^3$) (where X is C for *th* – C), and dihedral angles of Φ_{1234} and Φ_{5678}, which are depicted in Fig. 4 (a). For *th* – C, the d_1 and $d_2 = d_3$ increase with uniaxial-*x* tensile strain, leading to an increase in the *b* lattice constant. The α, β, Θ_{267}, Φ_{1234}, and the buckling thickness of h_1 and h_2 decreases whereas Φ_{5678} increases with increasing the stain, giving further insight into the projection of the bond length in the *xy*-plane. The increasing of the bond lengths, the decreasing of the buckling thickness, and especially the variation of dihedral angle of Φ_{1234} combined together act as the primary factors for the first decrease and then increase of the *b* lattice constant (Figure S8 (a) of Supporting Information). We further studied to reveal how the simultaneous increase in the lattice constant *a* of *th* – C emerges with the uniaxial-*y* strain. The variation of the lattice constant *a* is positively correlated the variation of the d_2 and its projection angles in the *xy*-plane. With the uniaxial-*y* strain, the d_2 and all the corresponding angles increase except for the dihedral angle of Φ_{1234} which first increases and then decreases (Figure S8 (b) of Supporting Information). The variation of the lattice constant *a* is dominated by the variation of Φ_{1234}, resulting in the emerged negative PR. Likewise, for *th* – XC compounds, the increasing of the bond lengths, the decreasing of the buckling thickness, and especially the variation of dihedral angle of Φ_{1234} combined together act as the primary factors for the emergence of the negative PR (Figure S9–S12 of Supporting Information). To clearly show the variation of the lattice constant *a*, we examine the variation of the moving direction of the atoms with respect to the uniaxial-*y* strain. For *th* – SiC, the moving direction of 3-fold coordinated carbon atoms simultaneously changed after the corresponding threshold strain value (Figure S9 of Supporting Information). Thus, the 2D carbides exhibit a sign-tunable in-plane Poisson's ratio depending on the imposed strain rate and direction. Although the unstrained 2D carbides are non-*auxetic* (positive PR), there exist auxetic (negative PR) effect under strain conditions. We clearly showed that the 2D carbides can be obtained as non-*auxetic*, *auxetic*, and partially *auxetic* (positive PR for some direction and negative PR for other ones). All these exceptional mechanical properties make the 2D tetrahex carbides useful for their potential as *auxetic* low-dimensional materials.

3.6.3. Ultimate tensile strength

In addition to in-plane stiffness, ideal strength [71] as an inherent mechanical property of materials is of great interest in material science. We investigated the ideal strength of the 2D carbides by analyzing the variation of stress with axial tensile strains using 2 × 2 supercell. The stress-strain curve of *th* – C and *th*"TT5843c571""ADXC compounds is presented in Fig. 5 where the upper limit of the stress is regarded as ultimate tensile strength (UTS) or ideal strength. The obtained UTS for uniaxial-*x* and uniaxial-*y*, and equi-biaxial strains (denoted as UTS^x, UTS^y, and UTS^{xy}, respectively) is summarized in Table 2. For *th* – C, the UTS^x, UTS^y, and UTS^{xy} are found to be 32%, 31%, and 20%, respectively, suggesting an excellent stretchability. Worthy to remind that the UTS of graphene, pentagraphene, and hexagonal boron nitride was reported as ~27% [72], 21% [57], and 30% [73], respectively, which are relatively lower than the UTS of most of the presented 2D carbides. Therefore, the 2D carbides exhibit ultrahigh ideal strength and good ductility playing an important role for the mechanical properties of 2D materials.

3.7. Electronic structures and photocatalytic properties for water splitting

To probe the electronic properties of the 2D tetrahex carbides, we investigated the electronic band structure, the charge distribution at conduction band minimum (CBM) and valence band maximum (VBM), and the corresponding partial density of states (PDOS). The electronic structures of *th* – C and *th* – XC compounds along the high symmetry directions of the BZ were calculated by the HSE06 functional and shown in Fig. 6 (upper panel). According to the band gap energies, summarized in Table 1, the 2D carbides are obviously natural semiconductors with desirable band gaps. The *th* – C possesses a direct band gap of 2.63 eV at the HSE06 functional where the CBM and VBM are located at the Γ high-symmetry point in the BZ. For *th* – XC compounds, the HSE06 predicted band gaps are in the range of 1.28–1.78 eV, which is an excellent range for potential use in applications such as nanoelectronics and solar cell devices. The charge density of the CBM and VBM for *th* – XC compounds is primarily localized on 3-fold coordinated atoms (X^3 and C^3) (Fig. 6, lower panel). The result of PDOS is further verified that the strong contribution to the electronic states is due to the p_z orbitals of X^3 and C^3 atoms with the small contributions of the X^4 and C^4 ones (Figure S13 of Supporting Information).

For a semiconductor to be an efficient photocatalyst for water splitting, several conditions simultaneously need to be satisfied. First, the band gap energy must exceed the free energy of water splitting (1.23 eV) and should be smaller than 3 eV to guarantee effective solar light absorption. Another requirement is that, the band edges must range over the redox potential of water splitting: that is, the conduction band edge position must be higher than the reduction potential of H^+/H_2 (-4.44 eV + pH × 0.059 eV) and the valence band edge position must be lower than the oxidation potential of O_2/H_2O (-5.67 eV + pH × 0.059 eV). For the band gap requirement of photocatalytic reaction, the proposed 2D tetrahex carbides appear to be a very promising for photocatalyst performance. We further aligned the band edges to the vacuum level with the HSE06 functional and compared with the redox potentials of water splitting in Fig. 7. The band edge positions of *th* – C, *th* – SiC, *th* – GeC, and their ternary alloys, namely th – $Si_{0.33}Ge_{0.67}C$ and th – $Si_{0.67}Ge_{0.33}C$, satisfy the band edge requirement for water splitting in the acidic environment (pH = 0). Although Sn-based ternary alloys, namely *th* – $Si_{0.67}Sn_{0.33}C$ and *th* – $Ge_{0.67}Sn_{0.33}C$, seem to be not suitable for water splitting at their equilibrium state due to the relatively lower position of CBM with respect to the reduction potential of H^+/H_2 (at pH = 0), both would straddle the water reduction and oxidation potentials by strain engineering, which is further elucidated below. It is worth noting that the position of VBM and CBM for the 2D tetrahex carbides is relatively lower than the oxygen evolution potential and higher than the

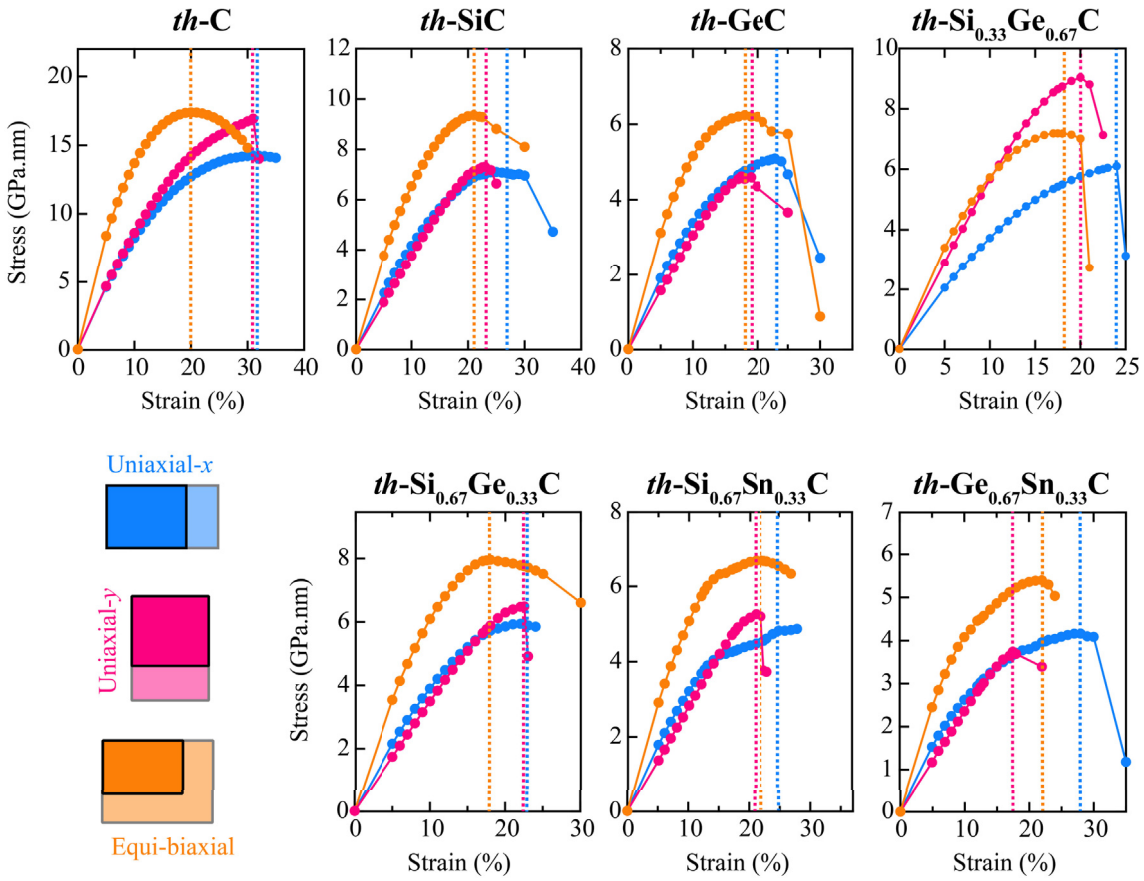

Fig. 5. Stress-strain relationship for uniaxial tensile strain in the *x* and *y* lattice directions (uniaxial-*x* and uniaxial-*y*) and equi-biaxial tensile strain for *th* – C and *th* – XC compounds. The maximal tensile stress (or ultimate tensile strength, UTS) points for each considered systems are depicted by dashed lines. Sky blue, pink, and orange colors represent for uniaxial-*x*, uniaxial-*y*, and equi-biaxial strains, respectively. (A colour version of this figure can be viewed online.)

hydrogen evolution potential, respectively, which would cause a low activity for water splitting. To assess the proper potential level, the modulation of band edges is here considered by two effective methods: alloying and strain engineering.

3.8. Tuning of the band gap and band edge positions of th – XC compounds by alloying and strain-engineering

Tailoring the electronic properties of semiconductor nanomaterials is of crucial interest for their potential applications. In our previous studies, we have found that the chemical functionalization and strain engineering are the effective strategies to enhance the electronic properties of *th* – C [37,38]. Herein, we investigated the influence of alloying and strain engineering on the electronic properties of the 2D carbides. Referring to Figs. 6 and 7, we conclude that the electronic band gap energy and band edge positions of the 2D tetrahex carbides can be systematically tuned by varying the ratio of group-IV elements (C, Si, Ge, Sn) in the tetrahexagonal lattice. For instance, the HSE06 functional band gap of *th* – $Si_{0.33}Ge_{0.67}C$ (1.45 eV) and *th* – $Si_{0.67}Ge_{0.33}C$ (1.53 eV) is in between that of *th* – SiC (1.78 eV) and *th* – GeC (1.34 eV), and remarkably the position of band edges can be adjusted by the ratio of Si and Ge atoms. Moreover, the direct band gap feature of *th* – $Si_{0.67}Sn_{0.33}C$ revealed that an indirect-to-direct band gap transition can be obtained by substituting 4-fold coordinated Si atoms in *th* – SiC with Sn atoms. Thus, the alloying additions of the group-IV elements in *th* – XC would offer a continuous band gap energy, the band-edge modulation, and band gap transition.

Following the exhibition of the ability to engineer the electronic properties of the 2D carbides by alloying, we examine the electronic property-strain relationship. We systematically investigated the strain-engineering band gap and band alignment of the 2D tetrahex carbides using the HSE06 functional. Fig. 8 exhibits the variation of the band gap with the position of the CBM and VBM as a function of uniaxial and biaxial strains from −2% to 10% with the increment of 2%. At each strain point, the atomic positions were first relaxed to the equilibrium positions, and then the corresponding band edge positions were obtained from the relaxed configurations. It is worth noting that the overall electronic band structures is not substantially modified by the application of strain (Figure S14 of Supporting Information). That is, the 2D tetrahex carbides remain semiconductor under considered magnitudes of strain although the strain has a significant effect on the band gap energy and band edge positions of the 2D tetrahex carbides. In general, for the case of uniaxial strain along the *x* direction, the band gap of 2D carbides steadily decreases with increasing tensile strain whereas it increases with compressive strain except for *th* – $Si_{0.67}Sn_{0.33}C$ where the compressive strain leads to the decrease in its band gap. For the uniaxial-*y* and biaxial strain, the band gaps increases with increasing the magnitude of the strain until reaching a maximum, and then decreases with further strain. In addition to the band gap energy, the position adjustment of the CBM and VBM levels of the 2D carbides depends linearly on the strain. The strain-imposed the 2D carbides is also quite exciting for photocatalytic water splitting. Remarkably, the band edge positions of *th* – $Si_{0.67}Sn_{0.33}C$ fit perfectly the redox potential level of water

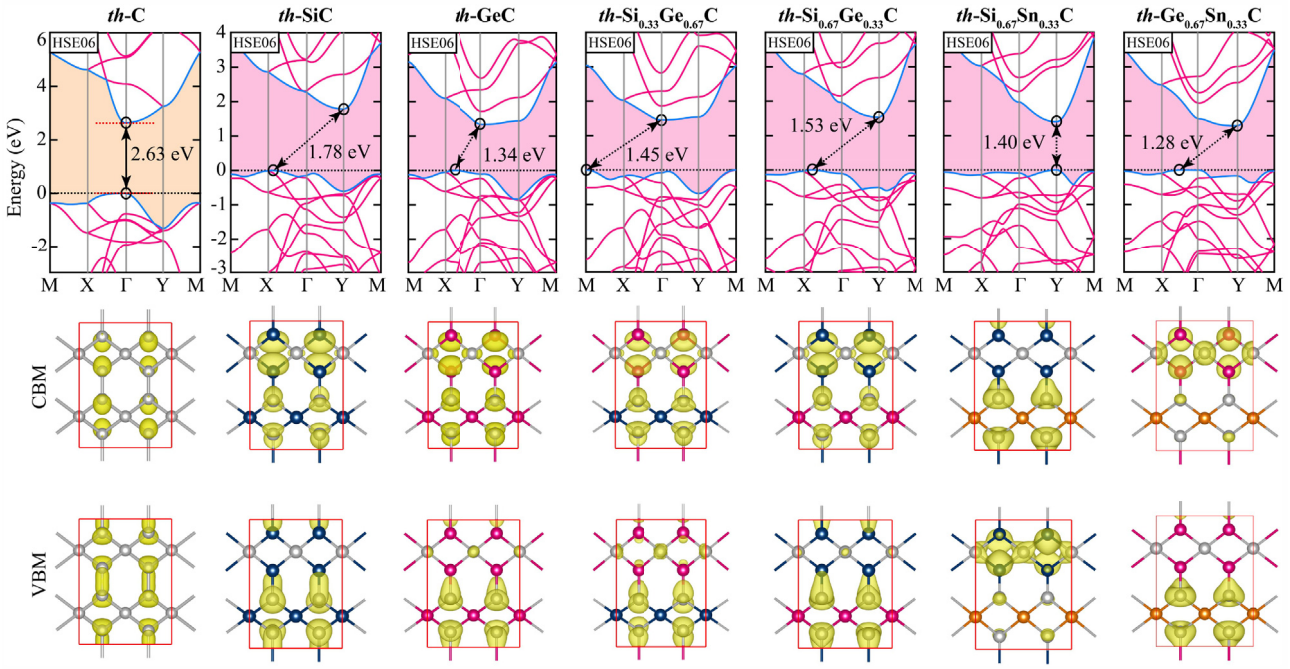

Fig. 6. Upper panels: Electronic band structure of *th* – C and *th* – XC compounds obtained from the HSE06 functional. Band widths between valence band maximum (VBM) and conduction band minimum (CBM) are shown with black arrows. The Fermi energy is set to zero, and depicted by the dashed black line. The fundamental band gap between the CBM and VBM of *th* – C and *th* – XC compounds are shaded orange and pink, respectively. Lower panels: Charge density of CBM and VBM of *th* – C and *th*"TT5843c571""ADXC compounds. Here, iso-surface of the charge density (yellow color lobes) is 0.005 e/Å^3. The gray, blue, pink, and orange balls represent C, Si, Ge, and Sn atoms, respectively. (A colour version of this figure can be viewed online.)

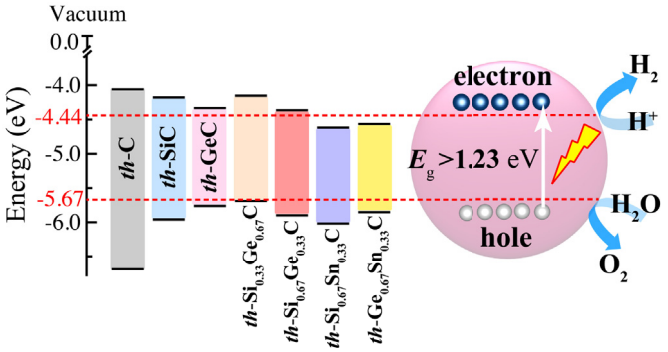

Fig. 7. (Left) Location of band-edges (CBM and VBM) of *th*"TT5843c571""ADC and *th*"TT5843c571""ADXC (X = Si, Ge, $Si_{0.33}Ge_{0.67}$, $Si_{0.67}Ge_{0.33}$, $Si_{0.67}Sn_{0.33}$, $Ge_{0.67}Sn_{0.33}$) with respect to vacuum level calculated with HSE06 functional. The redox potentials of water splitting are marked by the dashed red line at pH = 0. (Right) The working principle of water splitting with water reduction and oxidation potential levels. (A colour version of this figure can be viewed online.)

at 4–6% biaxial tensile strain, although its CBM is unable to derive the hydrogen evolution at its equilibrium state. Moreover, the band edge positions of *th*"TT5843c571""ADGe$_{0.67}$Sn$_{0.33}$C are slightly shifted to higher positions with respect to the redox potential of water under uniaxial-*y* tensile strain at 2–4%, rendering it useful in spontaneous photocatalytic water splitting. Clearly, the band gap and band edge positions of the 2D tetrahex carbides can be tuned by the application of strain, indicating their potential applications in nano- and opto-electronics.

3.9. Small effective mass and high carrier mobility

Inhibiting recombination and separation of photo-generated electron-hole pairs and prolonging the life time of charge carriers play a crucial role for efficient photocatalytic activity. To understand the mechanism of the migration and separation of the electron-hole pairs, we investigated the effective mass (m^*) and carrier transport (μ) of *th* – C and *th* – XC compounds. The effective mass of carriers was calculated by fitting the electronic band structure to a parabolic function using the following relation: $m^* = \hbar^2(d^2E(k)/dk^2)^{-1}$ where $\hbar$ is the reduced Planck constant and $d^2E(k)/dk^2$ is the second derivatives of the energy at the bottom of conduction band or the top of the valence bands with respect to wave vector *k*. The effective mass of electron (m_e^*) and hole (m_h^*) in terms of the free-electron mass (m_0) along the Γ"TT5843c571""ADX and Γ"TT5843c571""ADY directions are summarized in Table 3. The results indicate that *th* – C and *th* – XC compounds exhibit considerable anisotropy in the effective mass. To clearly show the anisotropy, we calculated direction-dependence of the effective mass of electron and hole for *th* – C from Γ"TT5843c571""ADX direction to Γ"TT5843c571""ADA an arbitrary direction (see Figure S15 (a) of Supporting Information). The effective mass of electron shows the smallest value of $0.11m_0$ in the *x* direction, while exhibits the largest value of $1.58m_0$ in the *y* direction. Also, from the electronic band structure of *th* – C, one can easily see that the curvature of band dispersion around the CBM in the *x* direction is much steeper than that in the *y* direction. Moreover, the large difference between the effective mass of electron and holes for *th* – C and *th* – XC compounds is observed in the *x* and *y* directions. This implies that the photo-induced electrons and holes move separately with a lower electron-hole recombination rate, which can significantly enhance the photocatalytic activity. We further calculated the carrier mobility along the most interesting directions (Γ"TT5843c571""ADX and Γ"TT5843c571""ADY directions) according to the formula: $\mu_i = \frac{eh^3C_i}{(2\pi)^3 k_B T m_i^* m_d E_{1i}^2}$ where *i* is

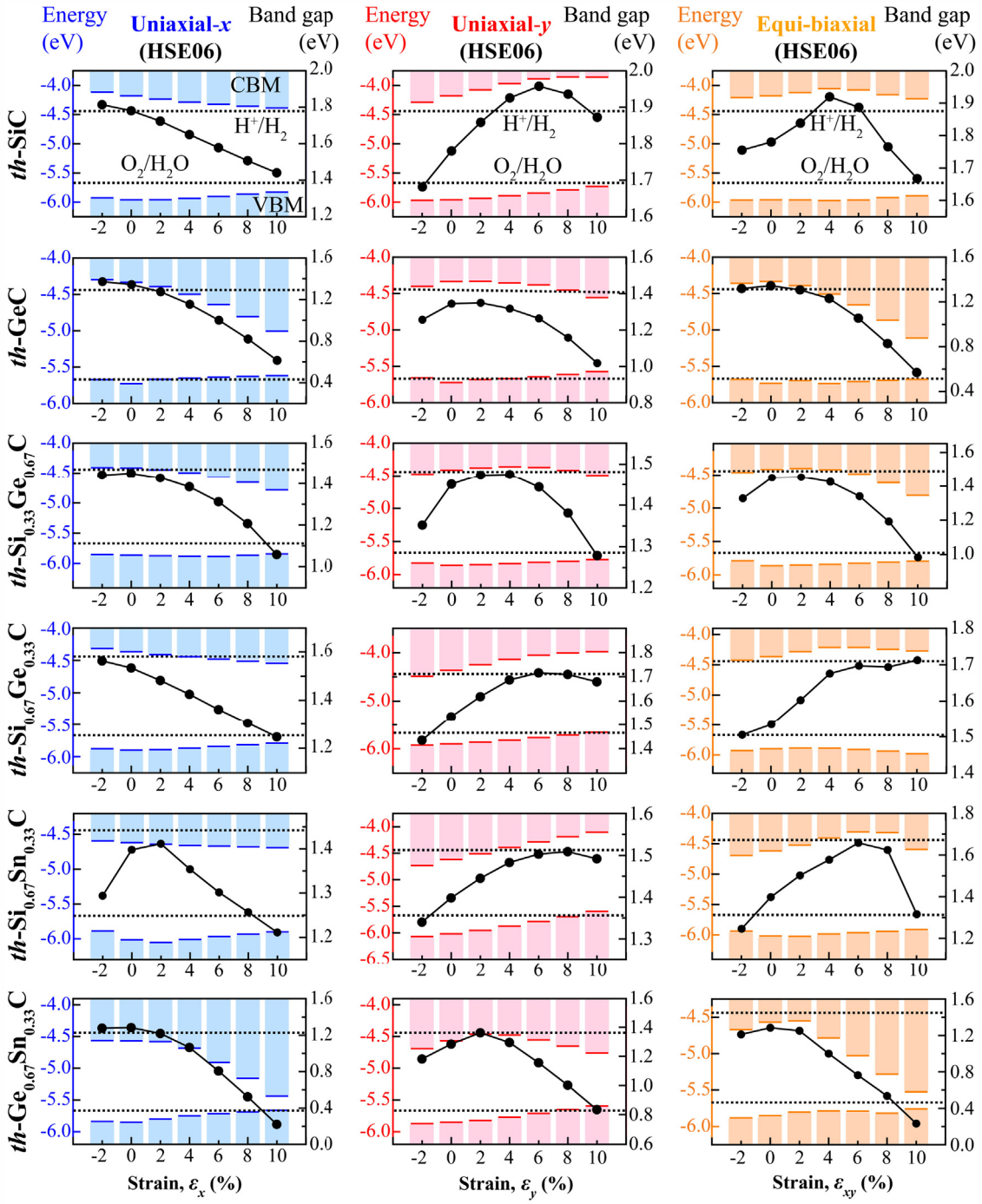

Fig. 8. HSE06 functional band gaps (black circle markers) and band edge positions (blue, pink, and orange bars for uniaxial-*x*, uniaxial-*y*, and biaxial strains, respectively) of $th-$XC compounds with respect to the vacuum level under strain from −2% to 10% (negative/positive numbers refer to as the compressive/tensile strain). The upper and lower colored bars represent the positions of the CBM and the VBM, respectively. The redox potentials of water splitting (black dashed line) are shown for comparison. (A colour version of this figure can be viewed online.)

the transport direction (x or y), m_i^* and $m_d = \sqrt{m_x^* m_y^*}$ are the effective mass along the transport direction i and the average effective mass, respectively. $E_{1i} = \Delta E/(\Delta l/l_0)$ is the deformation potential constant of the carrier where ΔE is the energy change of the VBM and CBM bands under small lattice strain (i.e. $\Delta l/l_0 = \pm$ 0.5% and ±1.0%), l_0 is the lattice constant along the transport direction i and presented in Figure S15 and Figure S16 of Supporting Information. Temperature is $T = 300$ K, C_i is the in-plane stiffness constant calculated from the equation $\frac{E_i - E_0}{A_0} = \frac{C_i}{2}\left(\frac{\Delta l}{l_0}\right)^2$ where E_0 and A_0 area and total energy of the unitcell. As listed in Table 3, $th-$C and $th-$XC compounds have high carrier mobilities, making them promising 2D materials for future applications in the electronic and optoelectronic field.

Table 3
Calculated carrier effective masses m^* (m_0 is the mass of a static electron), elastic constant C_{2D}, deformation potential constant E_1, and carrier mobility μ^{2D} of $th-$C and $th-$XC compounds along the x and y directions at $T = 300$ K.

2D material	Carrier type	m_x^*/m_0	m_y^*/m_0	C_{2D}^x (N/m)	C_{2D}^y (N/m)	E_1^x (eV)	E_1^y (eV)	μ_x^{2D} ($cm^2V^{-1}s^{-1}\times10^3$)	μ_y^{2D} ($cm^2V^{-1}s^{-1}\times10^3$)
$th-$C	Electron	0.11	1.58	287.03	280.82	5.08	2.23	5.00	1.81
	Hole	11.44	0.31	287.03	280.82	4.61	4.81	0.01	0.44
$th-$SiC	Electron	0.29	0.13	143.59	107.36	3.42	5.01	4.82	3.77
	Hole	0.96	0.21	143.59	107.36	1.01	0.60	7.05	67.11
$th-$GeC	Electron	0.33	18.94	119.15	84.18	2.89	2.44	0.37	0.01
	Hole	1.85	7.78	119.15	84.18	0.21	1.10	8.19	0.05
$th-Si_{0.33}Ge_{0.67}C$	Electron	0.56	16.67	126.97	97.24	0.82	1.75	2.34	0.01
	Hole	1.03	0.39	126.97	97.24	0.72	0.32	7.96	80.81
$th-Si_{0.67}Ge_{0.33}C$	Electron	0.23	0.24	135.12	94.46	2.77	5.37	6.89	1.25
	Hole	2.13	0.56	135.12	94.46	0.49	0.65	5.19	7.74
$th-Si_{0.67}Sn_{0.33}C$	Electron	0.25	0.22	115.86	75.95	1.71	4.89	14.25	1.30
	Hole	5.58	0.44	115.86	75.95	6.54	2.36	0.01	0.42
$th-Ge_{0.67}Sn_{0.33}C$	Electron	0.22	0.63	99.21	66.34	1.42	6.21	12.50	0.15
	Hole	16.76	0.36	99.21	66.34	1.76	0.79	0.02	2.56

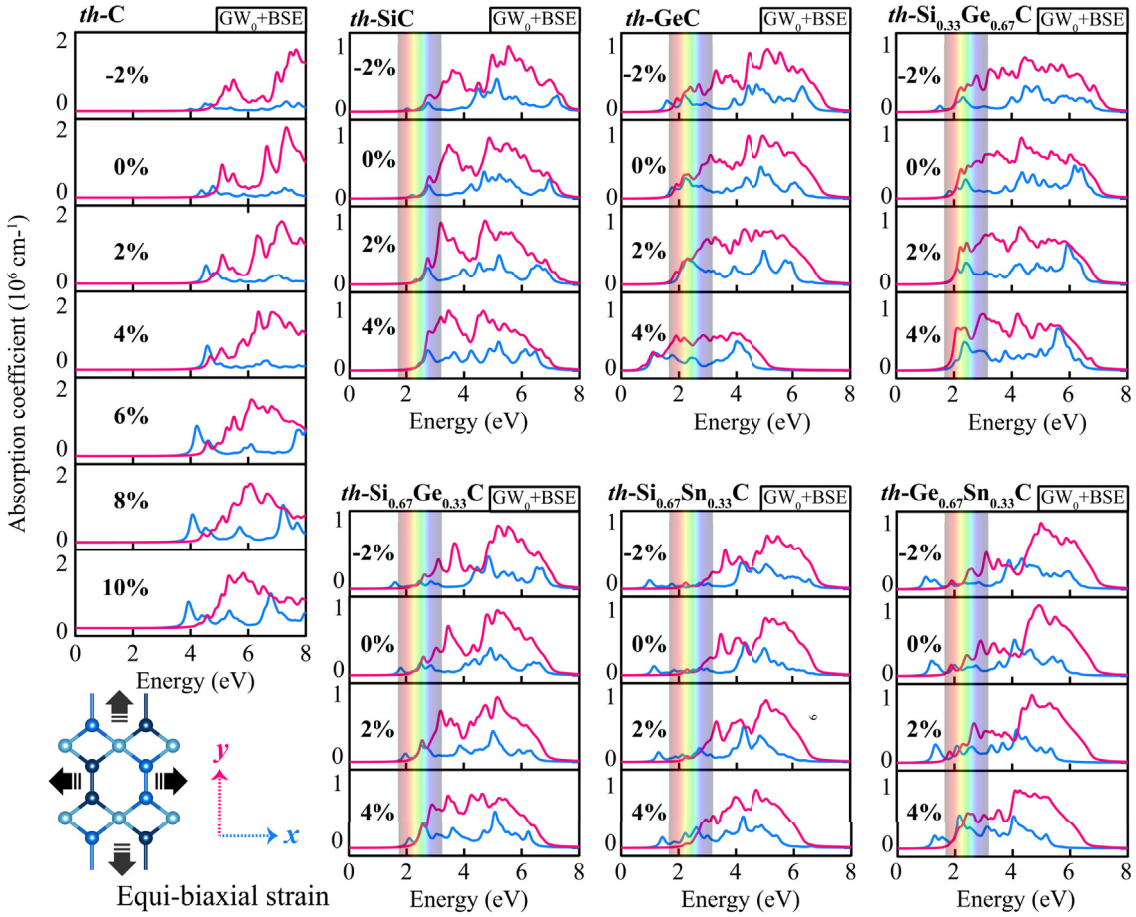

Fig. 9. The variation in optical absorption coefficient of $th-$C and $th-$XC (X = Si, Ge, $Si_{0.33}Ge_{0.67}$, $Si_{0.67}Ge_{0.33}$, $Si_{0.67}Sn_{0.33}$, $Ge_{0.67}Sn_{0.33}$) along the x and y (in-plane) lattice directions as a function of photon energy under different equi-biaxial tensile strains using the GW_0 + BSE method. The area between the red and purple represents the visible-light range. (A colour version of this figure can be viewed online.)

3.10. Optical properties

Besides a proper band alignment and suitable band gap, the light absorption capability is an important factor for photocatalyst in practical applications. In principle, the ultraviolet-based photocatalysts would exhibit a better performance than the visible light-based ones as ultraviolet light has much higher photonic energy than visible light. However, ultraviolet covers only 4% of the solar spectrum. Hence, the photocatalysts materials capturing a significant fraction of the visible spectrum (~43% of the solar spectrum) as opposed to by ultraviolet light are of great importance for solar cell applications. To evaluate the light harvesting performance of the 2D tetrahex carbides, we calculated their absorption coefficient by employing the state-of-the-art GW_0 + BSE method. The optical

absorption coefficient of the 2D carbides with polarization vectors parallel to the layer plane is presented in Fig. 9. The 2D carbides exhibit highly anisotropic absorption of light due to the structure anisotropy. The anisotropic optical response enables manipulation of light propagation properties, which is desirable for optoelectronic devices. For *th* – C, the strong optical absorption in ultraviolet spectral region was observed. With the application of tensile strain, the main absorption peaks of *th* – C are shifted to lower energy. For *th* – SiC, *th* – GeC, and their alloys (*th* – $Si_{0.33}Ge_{0.67}C$ and *th* – $Si_{0.67}Ge_{0.33}C$), the prominent optical absorbance was detected in the visible-ultraviolet spectrum. Under tensile strain, the main absorption peaks in *th* – SiC are shifted to higher energy whereas they moved to lower energy in *th* – GeC. Sn-based ternary alloys (*th* – $Si_{0.67}Sn_{0.33}C$ and *th* – $Ge_{0.67}Sn_{0.33}C$) exhibit the absorption peaks in the infrared, visible and ultraviolet regions, indicating their the wide absorption range. Remarkably, controlling the absorption edges in the wide optical absorption range from near-infrared to the visible region by alloying and strain engineering make the 2D tetrahex carbides potential for practical applications in optoelectronic devices. Our results show that the 2D carbides could absorb significant light energy over the entire solar spectrum, which greatly would facilitate their utilization as water splitting photocatalysts.

4. Conclusion

We computationally designed a series of new 2D group-IV carbides using first-principles calculations and revealed their energetic, dynamic, thermal, and mechanical stability by evaluating the formation energy, phonon dispersion, ab-initio molecular dynamics (AIMD) simulations, and elastic constants, respectively, suggesting that the realization of the 2D tetrahex carbides is likely. Their mechanical, electronic, and optical properties are found to be highly anisotropic. The 2D tetrahex carbides possess ultra-high strength and exhibit the sign tunable Poisson's ratio (PR). The negative Poisson's ratio (PR) in the 2D tetrahex carbides emerges by small tensile strain (2–5%). They can be obtained as non-auxetic, auxetic, and partially auxetic by strain engineering. The 2D tetrahex carbides are natural semiconductors with direct and indirect band gaps. Since the absence of band gap in 2D group-IV monoelemental materials sets limitations on their practical applications, the 2D tetrahex carbides would be promising to overcome this limitation. The electronic band gap energy and band edge positions of the 2D tetrahex carbides can be systematically tuned by varying the ratio of group-IV elements (C, Si, Ge, Sn) in the tetra-hexagonal lattice and strain engineering. The alloying also offers an indirect-to-direct band gap transition. The 2D tetrahex carbides exhibit high and directionally anisotropic carrier mobility, favorable for the separation of photo-generated carriers (electrons and holes). The 2D tetrahex carbides present very good optical absorption performance in the visible-light region. The position of band edges in the 2D tetrahex carbides satisfy the water oxidation and reduction potentials. These excellent properties render the 2D tetrahex carbides potentially promising optoelectronic materials for photocatalytic water splitting. Our work opens a new avenue to explore 2D materials in broad applications such as nano-electronics, nanomechanics, or energy applications.

CRediT authorship contribution statement

Mehmet Emin Kilic: Conceptualization, Investigation, Writing - original draft, Writing - review & editing, Visualization. **Kwang-Ryeol Lee:** Supervision, Writing - review & editing.

Declaration of competing interest

The authors declare that they have no known competing financial interests or personal relationships that could have appeared to influence the work reported in this paper.

Acknowledgment

This research was supported by the Korea Research Fellowship Program funded by the Ministry of Science and ICT through the National Research Foundation of Korea (2020H1D3A1A02081517) and the Nano Materials Research Program through the Ministry of Science and IT Technology under project No. NRF-2016M3A7B4025402. The computing environment was prepared by Materials Square.

Appendix A. Supplementary data

Supplementary data to this article can be found online at https://doi.org/10.1016/j.carbon.2020.12.003.

References

[1] K.S. Novoselov, A.K. Geim, S.V. Morozov, D. Jiang, Y. Zhang, S.V. Dubonos, I.V. Grigorieva, A.A. Firsov, Electric field effect in atomically thin carbon films, Science 306 (5696) (2004) 666–669.
[2] K.S. Novoselov, A.K. Geim, S. Morozov, D. Jiang, M.I. Katsnelson, I. Grigorieva, S. Dubonos, A. Firsov, Two-dimensional gas of massless Dirac fermions in graphene, Nature 438 (7065) (2005) 197.
[3] B. Luo, G. Liu, L. Wang, Recent advances in 2d materials for photocatalysis, Nanoscale 8 (13) (2016) 6904–6920.
[4] S. Ipek, M. Kilic, A. Mogulkoc, S. Cahangirov, E. Durgun, Semiconducting defect-free polymorph of borophene: peierls distortion in two dimensions, Phys. Rev. B 98 (24) (2018) 241408.
[5] Z. Guo, J. Zhou, L. Zhu, Z. Sun, MXene: a promising photocatalyst for water splitting, J. Mater. Chem. 4 (29) (2016) 11446–11452.
[6] B. Sa, Y.-L. Li, J. Qi, R. Ahuja, Z. Sun, Strain engineering for phosphorene: the potential application as a photocatalyst, J. Phys. Chem. C 118 (46) (2014) 26560–26568.
[7] A.K. Singh, K. Mathew, H.L. Zhuang, R.G. Hennig, Computational screening of 2d materials for photocatalysis, J. Phys. Chem. Lett. 6 (6) (2015) 1087–1098.
[8] Y. Sun, H. Cheng, S. Gao, Z. Sun, Q. Liu, Q. Liu, F. Lei, T. Yao, J. He, S. Wei, Freestanding tin disulfide single-layers realizing efficient visible-light water splitting, Angew. Chem. 51 (35) (2012) 8727–8731.
[9] Y. Sun, Z. Sun, S. Gao, H. Cheng, Q. Liu, J. Piao, T. Yao, C. Wu, S. Hu, S. Wei, Fabrication of flexible and freestanding zinc chalcogenide single layers, Nat. Commun. 3 (1) (2012) 1–7.
[10] K. Takeda, K. Shiraishi, Theoretical possibility of stage corrugation in Si and Ge analogs of graphite, Phys. Rev. B 50 (20) (1994) 14916.
[11] E. Durgun, S. Tongay, S. Ciraci, Silicon and III-V compound nanotubes: structural and electronic properties, Phys. Rev. B 72 (7) (2005), 075420.
[12] G.G. Guzmán-Verri, L.L.Y. Voon, Electronic structure of silicon-based nanostructures, Phys. Rev. B 76 (7) (2007), 075131.
[13] S. Cahangirov, M. Topsakal, E. Aktürk, H. Şahin, S. Ciraci, Two-and one-dimensional honeycomb structures of silicon and germanium, Phys. Rev. Lett. 102 (23) (2009) 236804.
[14] P. Vogt, P. De Padova, C. Quaresima, J. Avila, E. Frantzeskakis, M.C. Asensio, A. Resta, B. Ealet, G. Le Lay, Silicene: compelling experimental evidence for graphenelike two-dimensional silicon, Phys. Rev. Lett. 108 (15) (2012) 155501.
[15] A. Fleurence, R. Friedlein, T. Ozaki, H. Kawai, Y. Wang, Y. Yamada-Takamura, Experimental evidence for epitaxial silicene on diboride thin films, Phys. Rev. Lett. 108 (24) (2012) 245501.
[16] L. Meng, Y. Wang, L. Zhang, S. Du, R. Wu, L. Li, Y. Zhang, G. Li, H. Zhou, W.A. Hofer, Buckled silicene formation on Ir (111), Nano Lett. 13 (2) (2013) 685–690.
[17] M. Dávila, L. Xian, S. Cahangirov, A. Rubio, G. Le Lay, Germanene: a novel two-dimensional germanium allotrope akin to graphene and silicene, New J. Phys. 16 (9) (2014), 095002.
[18] L. Li, S.-Z. Lu, J. Pan, Z. Qin, Y.-Q. Wang, Y. Wang, G.-Y. Cao, S. Du, H.-J. Gao, Buckled germanene formation on Pt (111), Adv. Mater. 26 (28) (2014) 4820–4824.
[19] F.-f. Zhu, W.-j. Chen, Y. Xu, C.-l. Gao, D.-d. Guan, C.-h. Liu, D. Qian, S.-C. Zhang, J.-f. Jia, Epitaxial growth of two-dimensional stanene, Nat. Mater. 14 (10) (2015) 1020–1025.
[20] S. Balendhran, S. Walia, H. Nili, S. Sriram, M. Bhaskaran, Elemental analogues of graphene: silicene, germanene, stanene, and phosphorene, Small 11 (6) (2015) 640–652.

[21] L. Seixas, J. Padilha, A. Fazzio, Quantum spin hall effect on germanene nanorod embedded in completely hydrogenated germanene, Phys. Rev. B 89 (19) (2014) 195403.
[22] M. Ezawa, Monolayer topological insulators: silicene, germanene, and stanene, J. Phys. Soc. Jpn. 84 (12) (2015) 121003.
[23] C.L. Freeman, F. Claeyssens, N.L. Allan, J.H. Harding, Graphitic nanofilms as precursors to wurtzite films: Theory, Phys. Rev. Lett. 96 (6) (2006), 066102.
[24] H. Şahin, S. Cahangirov, M. Topsakal, E. Bekaroglu, E. Akturk, R.T. Senger, S. Ciraci, Monolayer honeycomb structures of group-IV elements and III-V binary compounds: first-principles calculations, Phys. Rev. B 80 (15) (2009) 155453.
[25] T.-Y. Lü, X.-X. Liao, H.-Q. Wang, J.-C. Zheng, Tuning the indirect–direct band gap transition of SiC, GeC and SnC monolayer in a graphene-like honeycomb structure by strain engineering: a quasiparticle gw study, J. Mater. Chem. 22 (19) (2012) 10062–10068.
[26] S. Lin, Light-emitting two-dimensional ultrathin silicon carbide, J. Phys. Chem. C 116 (6) (2012) 3951–3955.
[27] S. Lin, S. Zhang, X. Li, W. Xu, X. Pi, X. Liu, F. Wang, H. Wu, H. Chen, Quasi-two-dimensional SiC and SiC2: interaction of silicon and carbon at atomic thin lattice plane, J. Phys. Chem. C 119 (34) (2015) 19772–19779.
[28] S. Chabi, H. Chang, Y. Xia, Y. Zhu, From graphene to silicon carbide: ultrathin silicon carbide flakes, Nanotech 27 (7) (2016), 075602.
[29] T. Susi, V. Skákalová, A. Mittelberger, P. Kotrusz, M. Hulman, T.J. Pennycook, C. Mangler, J. Kotakoski, J.C. Meyer, Computational insights and the observation of SiC nanograin assembly: towards 2D silicon carbide, Sci. Rep. 7 (1) (2017) 1–9.
[30] L.-J. Zhou, Y.-F. Zhang, L.-M. Wu, SiC2 siligraphene and nanotubes: novel donor materials in excitonic solar cells, Nano Lett. 13 (11) (2013) 5431–5436.
[31] Z. Shi, Z. Zhang, A. Kutana, B.I. Yakobson, Predicting two-dimensional silicon carbide monolayers, ACS Nano 9 (10) (2015) 9802–9809.
[32] L. Zhou, H. Dong, S. Tretiak, Recent advances of novel ultrathin two-dimensional silicon carbides from a theoretical perspective, Nanoscale 12 (2020) 4269–4282.
[33] B. Ram, H. Mizuseki, Tetrahexcarbon: a two-dimensional allotrope of carbon, Carbon 137 (2018) 266–273.
[34] F.M. de Vasconcelos, A.G. Souza Filho, V. Meunier, E.C. Girão, Electronic properties of tetragraphene nanoribbons, Phys. Rev. Mater. 3 (6) (2019), 066002.
[35] F.M. de Vasconcelos, A.G. Souza Filho, V. Meunier, E.C. Girão, Electronic and structural properties of tetragraphenes, Carbon 167 (2020) 403–413.
[36] Q. Wei, G. Yang, X. Peng, Auxetic tetrahex carbon with ultrahigh strength and a direct band gap, Phys. Rev. Appl. 13 (3) (2020), 034065.
[37] M.E. Kilic, K.-R. Lee, Tuning the electronic, mechanical, thermal, and optical properties of tetrahexcarbon via hydrogenation, Carbon 161 (2020) 71–82.
[38] M.E. Kilic, K.-R. Lee, First-principles study of fluorinated tetrahexcarbon: stable configurations, thermal, mechanical, and electronic properties, J. Phys. Chem. C 124 (2020) 8225.
[39] P.E. Blöchl, Projector augmented-wave method, Phys. Rev. B 50 (24) (1994) 17953.
[40] G. Kresse, D. Joubert, From ultrasoft pseudopotentials to the projector augmented-wave method, Phys. Rev. B 59 (3) (1999) 1758.
[41] G. Kresse, J. Hafner, Norm-conserving and ultrasoft pseudopotentials for first-row and transition elements, J. Phys. Condens. Matter 6 (40) (1994) 8245.
[42] J.P. Perdew, K. Burke, M. Ernzerhof, Generalized gradient approximation made simple, Phys. Rev. Lett. 77 (18) (1996) 3865.
[43] H.J. Monkhorst, J.D. Pack, Special points for Brillouin-zone integrations, Phys. Rev. B 13 (12) (1976) 5188.
[44] J. Heyd, G.E. Scuseria, M. Ernzerhof, Hybrid functionals based on a screened coulomb potential, J. Chem. Phys. 118 (18) (2003) 8207–8215.
[45] J. Paier, M. Marsman, K. Hummer, G. Kresse, I.C. Gerber, J.G. Ángyán, Screened hybrid density functionals applied to solids, J. Chem. Phys. 124 (15) (2006) 154709.
[46] L. Chaput, A. Togo, I. Tanaka, G. Hug, Phonon-phonon interactions in transition metals, Phys. Rev. B 84 (9) (2011), 094302.
[47] S. Nosé, A unified formulation of the constant temperature molecular dynamics methods, J. Chem. Phys. 81 (1) (1984) 511–519.
[48] S. Nosé, A molecular dynamics method for simulations in the canonical ensemble, Mol. Phys. 52 (2) (1984) 255–268.
[49] W.G. Hoover, Canonical dynamics: equilibrium phase-space distributions, Phys. Rev. A 31 (3) (1985) 1695.
[50] G. Onida, L. Reining, A. Rubio, Electronic excitations: density-functional versus many-body Greens-function approaches, Rev. Mod. Phys. 74 (2) (2002) 601.
[51] S. Albrecht, L. Reining, R. Del Sole, G. Onida, Ab initio calculation of excitonic effects in the optical spectra of semiconductors, Phys. Rev. Lett. 80 (20) (1998) 4510.
[52] M. Rohlfing, S.G. Louie, Electron-hole excitations in semiconductors and insulators, Phys. Rev. Lett. 81 (11) (1998) 2312.
[53] D. Fan, S. Lu, Y. Guo, X. Hu, Novel bonding patterns and optoelectronic properties of the two-dimensional Si x C y monolayers, J. Mater. Chem. C 5 (14) (2017) 3561–3567.
[54] G. Li, Y. Li, H. Liu, Y. Guo, Y. Li, D. Zhu, Architecture of graphdiyne nanoscale films, ChemComm 46 (19) (2010) 3256–3258.
[55] A. Molina-Sanchez, L. Wirtz, Phonons in single-layer and few-layer MoS2 and WS2, Phys. Rev. B 84 (15) (2011) 155413.
[56] M. Born, K. Huang, Dynamical Theory of Crystal Lattices, Clarendon press, 1954.
[57] S. Zhang, J. Zhou, Q. Wang, X. Chen, Y. Kawazoe, P. Jena, Penta-graphene: a new carbon allotrope, Proc. Natl. Acad. Sci. U. S. A 112 (8) (2015) 2372–2377.
[58] M. Manju, K. Ajith, M. Valsakumar, Strain induced anisotropic mechanical and electronic properties of 2D-SiC, Mech. Mater. 120 (2018) 43–52.
[59] Q. Peng, C. Liang, W. Ji, S. De, A first-principles study of the mechanical properties of g-GeC, Mech. Mater. 64 (2013) 135–141.
[60] K.E. Evans, M. Nkansah, I. Hutchinson, S. Rogers, Molecular network design, Nature 353 (6340) (1991) 124, 124.
[61] R. Lakes, Response: negative Poisson's ratio materials, Science 238 (4826) (1987) 551, 551.
[62] E. Friis, R. Lakes, J. Park, Negative Poisson's ratio polymeric and metallic foams, J. Mater. Sci. 23 (12) (1988) 4406–4414.
[63] G.N. Greaves, A. Greer, R.S. Lakes, T. Rouxel, Poisson's ratio and modern materials, Nat. Mater. 10 (11) (2011) 823–837.
[64] Q. Liu, Literature Review: Materials with Negative Poisson's Ratios and Potential Applications to Eerospace and Defence, Tech. Rep., Defence Science and Technology Organisation Victoria (Australia) Air, 2006.
[65] F. Scarpa, Auxetic materials for bioprostheses [in the spotlight], IEEE Signal Process. Mag. 25 (5) (2008) 128, 126.
[66] J.-W. Jiang, H.S. Park, Negative Poissons ratio in single-layer black phosphorus, Nat. Commun. 5 (1) (2014) 1–7.
[67] R. Pekoz, M. Konuk, M.E. Kilic, E. Durgun, Two-dimensional fluorinated boron sheets: mechanical, electronic, and thermal properties, ACS Omega 3 (2) (2018) 1815–1822.
[68] G. Qin, Z. Qin, Negative Poissons ratio in two-dimensional honeycomb structures, Npj Comput. Mater. 6 (1) (2020) 1–6.
[69] D.T. Ho, S.-D. Park, S.-Y. Kwon, K. Park, S.Y. Kim, Negative Poissons ratios in metal nanoplates, Nat. Commun. 5 (1) (2014) 1–8.
[70] J.-W. Jiang, H.S. Park, Negative Poissons ratio in single-layer graphene ribbons, Nano Lett. 16 (4) (2016) 2657–2662.
[71] T. Li, J. Morris Jr., N. Nagasako, S. Kuramoto, D. Chrzan, "ideal" engineering alloys, Phys. Rev. Lett. 98 (10) (2007) 105503.
[72] F. Liu, P. Ming, J. Li, Ab initio calculation of ideal strength and phonon instability of graphene under tension, Phys. Rev. B 76 (6) (2007), 064120.
[73] Q. Peng, W. Ji, S. De, Mechanical properties of the hexagonal boron nitride monolayer: ab initio study, Comput. Mater. Sci. 56 (2012) 11–17.